ARTICLE

https://doi.org/10.1007/s40820-025-01691-7

Host–Guest Inversion Engineering Induced Superionic Composite Solid Electrolytes for High-Rate Solid-State Alkali Metal Batteries

Xiong Xiong Liu[1], Long Pan[1] ✉, Haotian Zhang[1], Pengcheng Yuan[1], Mufan Cao[1], Yaping Wang[1], Zeyuan Xu[1], Min Gao[1], Zheng Ming Sun[1] ✉

HIGHLIGHTS

- Host–guest inversion engineering is proposed to create poly(vinylidene fluoride-hexafluoropropylene) (PVH)-in-SiO_2 composite solid electrolytes with an original "polymer guest-in-ceramic host" architecture, exhibiting optimized interfacial contacts and comprehensive properties.

- The PVH-in-SiO_2 exhibits an overwhelming ionic conductivity of 1.32×10^{-3} S cm^{-1} at 25 °C, with an ultralow residual solvent content of 2.9 wt%. In addition, the LiFePO$_4$|PVH-in-SiO_2|Li full cells deliver a significant capacity retention of 92.9% at an ultrahigh rate of 3C after 300 cycles at 25 °C.

- The host–guest inversion engineering is a versatile strategy, as proved by preparing Na$^+$ and K$^+$-based PVH-in-SiO_2 composite solid electrolytes, delivering excellent ionic conductivity of 10^{-4} S cm^{-1} at 25 °C (vs. 10^{-6}–10^{-5} S cm^{-1} of previous reports).

ABSTRACT Composite solid electrolytes (CSEs) are promising for solid-state Li metal batteries but suffer from inferior room-temperature ionic conductivity due to sluggish ion transport and high cost due to expensive active ceramic fillers. Here, a host–guest inversion engineering strategy is proposed to develop superionic CSEs using cost-effective SiO$_2$ nanoparticles as passive ceramic hosts and poly(vinylidene fluoride-hexafluoropropylene) (PVH) microspheres as polymer guests, forming an unprecedented "polymer guest-in-ceramic host" (i.e., PVH-in-SiO$_2$) architecture differing from the traditional "ceramic guest-in-polymer host". The PVH-in-SiO$_2$ exhibits excellent Li-salt dissociation, achieving high-concentration free Li$^+$. Owing to the low diffusion energy barriers and high diffusion coefficient, the free Li$^+$ is thermodynamically and kinetically favorable to migrate to and transport at the SiO$_2$/PVH interfaces. Consequently, the PVH-in-SiO$_2$ delivers an exceptional ionic conductivity of 1.32×10^{-3} S cm^{-1} at 25 °C (vs. typically 10^{-5}–10^{-4} S cm^{-1} using high-cost active ceramics), achieved under an ultralow residual solvent content of 2.9 wt% (vs. 8–15 wt% in other CSEs). Additionally, PVH-in-SiO$_2$ is electrochemically stable with Li anode and various cathodes. Therefore, the PVH-in-SiO$_2$ demonstrates excellent high-rate cyclability in LiFePO$_4$|Li full cells (92.9% capacity-retention at 3C after 300 cycles under 25 °C) and outstanding stability with high-mass-loading LiFePO$_4$ (9.2 mg cm^{-1}) and high-voltage NCM622 (147.1 mAh g^{-1}). Furthermore, we verify the versatility of the host–guest inversion engineering strategy by fabricating Na-ion and K-ion-based PVH-in-SiO$_2$ CSEs with similarly excellent promotions in ionic conductivity. Our strategy offers a simple, low-cost approach to fabricating superionic CSEs for large-scale application of solid-state Li metal batteries and beyond.

KEYWORDS Host–guest inversion engineering; SiO$_2$ nanoparticle; Superionic conductivity; Composite solid electrolyte; Solid-state alkali metal battery

Xiong Xiong Liu and Long Pan have contributed equally to this work.

✉ Long Pan, panlong@seu.edu.cn; Zheng Ming Sun, zmsun@seu.edu.cn

1 School of Materials Science and Engineering, Southeast University, Nanjing 211189, People's Republic of China

1 Introduction

The ever-growing anxieties about the battery life and safety of liquid lithium-ion batteries are boosting the flourishing development of solid-state Li metal batteries as they can simultaneously improve energy density and inhibit thermal runaway [1–3]. Solid-state electrolytes are fundamental to solid-state Li metal batteries, requiring decent interfacial contacts, high mechanical modulus, wide electrochemical window, and, in particular, high ionic conductivity (at least 10^{-3} S cm^{-1} at room temperature) to meet practical applications [4–6]. In this sense, composite solid-state electrolytes (CSEs), which are commonly comprised of active ceramics as fillers (i.e., guests) and polymers as matrices (i.e., hosts) to form traditional "ceramic guest-in-polymer host" architectures, have provoked significant interest. Because active ceramic guests are ion-conducting, CSEs can integrate the high modulus and ionic conductivity of active ceramic guests with the excellent processability and interfacial compatibility of polymer hosts [7, 8]. To date, various active ceramic guests have been introduced, including oxides (e.g., $Li_7La_3Zr_2O_{12}$) [9–13], sulfides (e.g., Li_6PS_5Cl) [14, 15], and phosphates (e.g., $Li_{1.3}Al_{0.3}Ti_{1.7}(PO_4)_3$) [16, 17]. However, CSEs based on active ceramic guests are still far from practical applications because of their insufficient ionic conductivities (generally 10^{-5}–10^{-4} S cm^{-1} at room temperature) [18–20]. Another critical challenge is induced by the high cost, harsh synthesis, and complex handling of active ceramic guests [21, 22].

To address these problems, passive ceramics, which are not ion conductors, have been proposed as guests to incorporate with polymer hosts, including SiO_2, Al_2O_3, TiO_2, etc.[23, 24]. Compared to active ceramics, passive ceramics possess advantages such as lower cost, simpler preparation, easier handling, and better environmental compatibility. These merits make passive ceramics particularly appealing for large-scale applications of CSEs [25]. More importantly, CSEs based on passive ceramics exhibit comparable ionic conductivities (10^{-5}–10^{-4} S cm^{-1} at room temperature) to those based on active ceramics [26, 27]. Therefore, it is of significant importance to develop next-generation passive ceramic-based CSEs to achieve superionic conductivity (at least 10^{-3} S cm^{-1}) at room temperature.

Although passive ceramics are not ion-conducting, they have strong interfacial Lewis acid–base interactions with Li salts, thereby expediting the dissociation of Li salts [28]. They can also weaken polymer crystallization, producing more amorphous regions to boost Li$^+$ transport [29]. Furthermore, recent theoretical calculations revealed that the interfacial ionic conductivity between ceramics and polymers can reach as high as 10^{-2} S cm^{-1} (at 30 °C) [30]. These findings, therefore, inspire that maximizing the ceramic/polymer interfacial contacts can promise adequate moveable ions with superionic conductivities at room temperature. In this circumstance, increasing the weight ratio of ceramic guests and polymer hosts (up to 400 wt%) has been proposed to increase the interfacial contacts [31]. Despite the high content of ceramic guests, only conventional "ceramic guest-in-polymer host" architectures were obtained with limited interfacial contacts (Fig. S1), because ceramics typically have much higher densities than polymers and exhibit micron-order particle sizes (Table S1). Accordingly, increasing the content of ceramic guests only leads to limited progress in ionic conductivity (10^{-4} S cm^{-1} at room temperature) [31–36]. Therefore, building advanced CSEs with novel host–guest architectures to achieve optimized interfacial contacts and continuous ion pathways is a fundamental challenge rather than simply improving the content of passive ceramic guests.

In this contribution, we, for the first time, propose a host–guest inversion engineering to realize superionic CSEs composed of monodisperse SiO_2 nanoparticles and poly(vinylidene fluoride-hexafluoropropylene) (PVH) microspheres. Note that SiO_2 is a typical passive ceramic and serves as the host in our case rather than the traditional guest because of its relatively low density to boost the volume-to-weight ratio (Table S1). In addition, SiO_2 shows the merits of low cost, facile preparation, and environmental friendliness. Correspondingly, PVH serves as the guest instead of the traditional host because it favors forming interconnected sphere scaffolds (Fig. 1a). In particular, PVH exhibits a relatively high density that can lower its volume-to-weight ratio, leaving continuous voids with large volumes for filling SiO_2 nanoparticle hosts. Moreover, PVH shows high mechanical strength and excellent dielectric constant that facilitates the dissociation of alkali metal salt [37]. As a result, the obtained CSEs undergo an architecture inversion from the traditional "ceramic guest-in-polymer host" (i.e., "SiO_2-in-PVH") (Fig. 1b) to the innovative "polymer guest-in-ceramic host" (i.e., "PVH-in-SiO_2") (Fig. 1c) when

the SiO_2/PVH weight ratio increases from 20/100 to 70/100. Such ratio is much lower than previous reports, which have a ceramic/polymer weight ratio of up to 400/100. For simplification and clarification, the terms "PVH", "SiO_2-in-PVH", and "PVH-in-SiO_2" are used throughout the manuscript for the CSEs with SiO_2/PVH weight ratio of 0/100, 20/100, and 70/100, respectively.

Benefiting from the unprecedented PVH-in-SiO_2 architecture, the PVH microspheres are densely covered by numerous SiO_2 nanoparticles, maximizing the SiO_2/PVH interfacial contacts and creating continuous interfacial pathways for fast ion transport (Fig. 1c). As a result, the PVH-in-SiO_2 delivers an unexceptionally high ionic conductivity of 1.32×10^{-3} S cm^{-1} at 25 °C under an extremely low residual solvent content (2.9 wt%, calculated based on the total weight

loss from ambient temperature to 200 °C), overwhelming most recently reported CSEs and polymer solid-state electrolytes (PSEs) (Fig. 1d and Table S2) [26, 28, 38–52]. The PVH-in-SiO_2 also features easy handling, flexibility, and scalability (Fig. 1e), which is essential for their large-scale implementation in practical solid-state Li metal batteries. In addition, the PVH-in-SiO_2 shows outstanding electrochemical stability against Li metal with a cycling life of more than 1000 h at the current density of 0.2 mA cm^{-2}. Moreover, the LiFePO$_4$|PVH-in-SiO_2|Li solid-state full cells exhibit excellent rate capability and cycling stability, with a remarkable capacity retention of 92.9% at a high current density of 3C after 300 cycles under 25 °C, surpassing many recently reported LiFePO$_4$|Li solid-state full cells. The PVH-in-SiO_2 also demonstrates good cyclability and safety when using
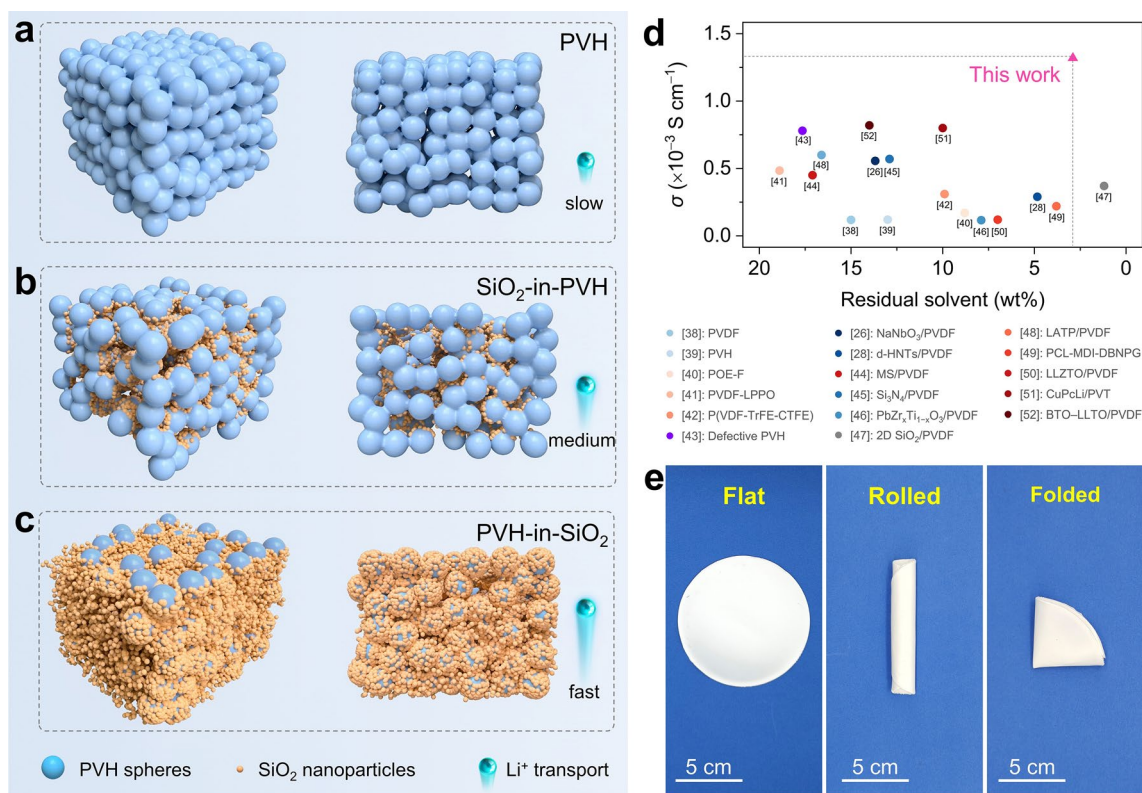
Fig. 1 Structure and ion transport performance of PVH-in-SiO_2. **a–c** Illustration of structures and ion-conducting behaviors of **a** PVH, **b** SiO_2-in-PVH, and **c** PVH-in-SiO_2. The PVH forms interconnected micron-sized spheres (blue balls), in which SiO_2 nanoparticles (orange balls) are filled into the voids, forming SiO_2-in-PVH or PVH-in-SiO_2 architectures by varying the SiO_2 content. Note that ions transport sluggishly inside the polymer but show high theoretical conductivity (up to 10^{-2} S cm^{-1}) at the ceramic/polymer interfaces [30]. Therefore, the PVH-in-SiO_2 shows fast ion diffusion at the SiO_2/PVH interfaces because PVH spheres are densely covered by SiO_2 nanoparticles, forming continuous interfacial ion-conducting highways. **d** Comparison of ionic conductivity (at 25 °C) and residual solvent content of our PVH-in-SiO_2 with other reported CSEs and PSEs [26, 28, 38–52]. Although the residual solvent is favorable for ion conduction, it seriously affects Li metal anodes and battery safety. Therefore, our PVH-in-SiO_2 efficiently addresses the residual solvent problems without compromising the superionic capability. **e** Digital photographs of a sizeable and flexible PVH-in-SiO_2 film with a diameter of 11 cm. (Color figure online)

high-mass-loading LiFePO$_4$ (9.2 mg cm^{-2}) and high-voltage NCM622 cathodes (147.1 mAh g^{-2} at 0.2C after 100 cycles). More impressively, we verify that the host–guest inversion engineering strategy is general and can be extended to preparing advanced Na-ion and K-ion-based CSEs by simply replacing Li salt with its counterparts (i.e., Na and K salts). The resulting PVH-in-SiO$_2$-Na and PVH-in-SiO$_2$–K exhibit exciting ionic conductivities of 3.03×10^{-4} and 2.56×10^{-4} S cm^{-1} (14 and 64 times that of PVH-Na and PVH-K at 25 °C), respectively. The PVH-in-SiO$_2$-Na and PVH-in-SiO$_2$-K also showcase outstanding full-cell cycling stability with 86.4% and 84.3% capacity retention after 500 cycles at the current density of 0.5C under 25 °C. Our host–guest inversion engineering strategy opens a new avenue for using passive ceramics to develop low-cost and scalable high-performance CSEs, promising the practical applications of next-generation solid-state alkali metal batteries.

2 Results and Discussion

2.1 Synthesis, Morphology, and Properties of PVH-in-SiO$_2$

The preparation process is depicted in Fig. 2a, b, before which monodisperse SiO$_2$ nanoparticles with an average diameter of 158 nm were synthesized by an efficient hydrolysis approach (Figs. 2c and S2, S3) [53]. PVH-in-SiO$_2$ films were fabricated using a simple solution casting approach, through which the SiO$_2$ nanoparticles and PVH were mixed at the weight ratio of 70/100. Control samples, viz., PVH and SiO$_2$-in-PVH films, were also prepared using the same procedure, except that the SiO$_2$/PVH weight ratios were 0/100 and 20/100, respectively.

To reveal the morphological information of the as-prepared CSE films, scanning electron microscopy (SEM) was employed. Figures 2d and S4, S5 show the SEM images of PVH, in which 2.9 μm spheres are formed and interconnected, leaving abundant voids. When a small ratio of SiO$_2$ nanoparticles is introduced (i.e., SiO$_2$/PVH = 20/100), they partially occupy the voids and loosely cover the PVH spheres (Figs. 2e and S6, S7). As a result, a traditional "creamic guest-in-polymer host" architecture (i.e., SiO$_2$-in-PVH in our case) is generated, leading to insufficient and discontinuous PVH/SiO$_2$ interfacial contacts that are unfavorable for fast Li$^+$ conducting (as discussed later). As the SiO$_2$/

PVH weight ratio increases to 70/100, the PVH spheres are immersed in the "sea" of SiO$_2$ nanoparticles, forming an innovative "polymer host-in-creamic guest" architecture (i.e., PVH-in-SiO$_2$ in our case), as Figs. 2f and S8, S9 show. With this architecture, the PVH surfaces are entirely covered by SiO$_2$ nanoparticles, resulting in adequate and continuous interfacial contacts and pathways for fast Li$^+$ conduction.

The superionic properties of PVH-in-SiO$_2$ were comprehensively evaluated by investigating its ionic conductivity, activation energy, and Li$^+$ transference number. Figures 2g and S10 show that the PVH-in-SiO$_2$ exhibits an outstanding ionic conductivity of 1.32×10^{-3} S cm^{-1} at 25 °C, which is an order of magnitude higher than PVH (3.7×10^{-4} S cm^{-1}) and SiO$_2$-in-PVH (5.9×10^{-4} S cm^{-1}). The ionic conductivity results indicate that the PVH-in-SiO$_2$ architecture can significantly facilitate the LiTFSI dissociation and ion mobility, which is further validated by calculating activation energies using the Arrhenius equation (Figs. 2h and S11). The PVH has a high activation energy of 0.22 eV, which quickly declined to 0.17 eV in the case of PVH-in-SiO$_2$, implying that PVH-in-SiO$_2$ possesses the lowest energy barrier for ion mobility. This energy barrier is also smaller than those reported previously (Table S3) [26, 28, 38–43, 45–48, 50, 52]. In addition, the PVH-in-SiO$_2$ also has a large Li$^+$ transference number of 0.46, which is approximately 2.4 and 1.4 times that of PVH and SiO$_2$-in-PVH (Figs. 2i and S12), suggesting that the PVH-in-SiO$_2$ architecture is more favorable for boosting the mobility of Li$^+$ instead of its counterion (i.e., TFSI$^-$) [54]. Moreover, we stress that the superionic properties of PVH-in-SiO$_2$ are not attributed to the residual solvent because the total residual solvent is only 2.9 wt% (Fig. S13), which is significantly lower than previous reports (generally > 10 wt%, Fig. 1d and Table S2) [26, 28, 38–52]. Such a low residual solvent content can minimize the side reactions between solvent and Li metal anodes, thereby achieving good cycling stability in both Li-based symmetric and full cells (as proved and discussed later). In other words, our PVH-in-SiO$_2$ efficiently addresses the residual solvent problems without compromising the fast-ion-conducting capability.

The electrochemical oxidation stability of PVH-in-SiO$_2$ was initially investigated using linear sweeping voltammetry (LSV) at 25 °C, and the results are shown in Fig. 2j. In the case of PVH, a negligible oxidation peak is observed at approximately 4.00 V, after which the current starts to roar at 4.66 V, indicating that fast oxidation
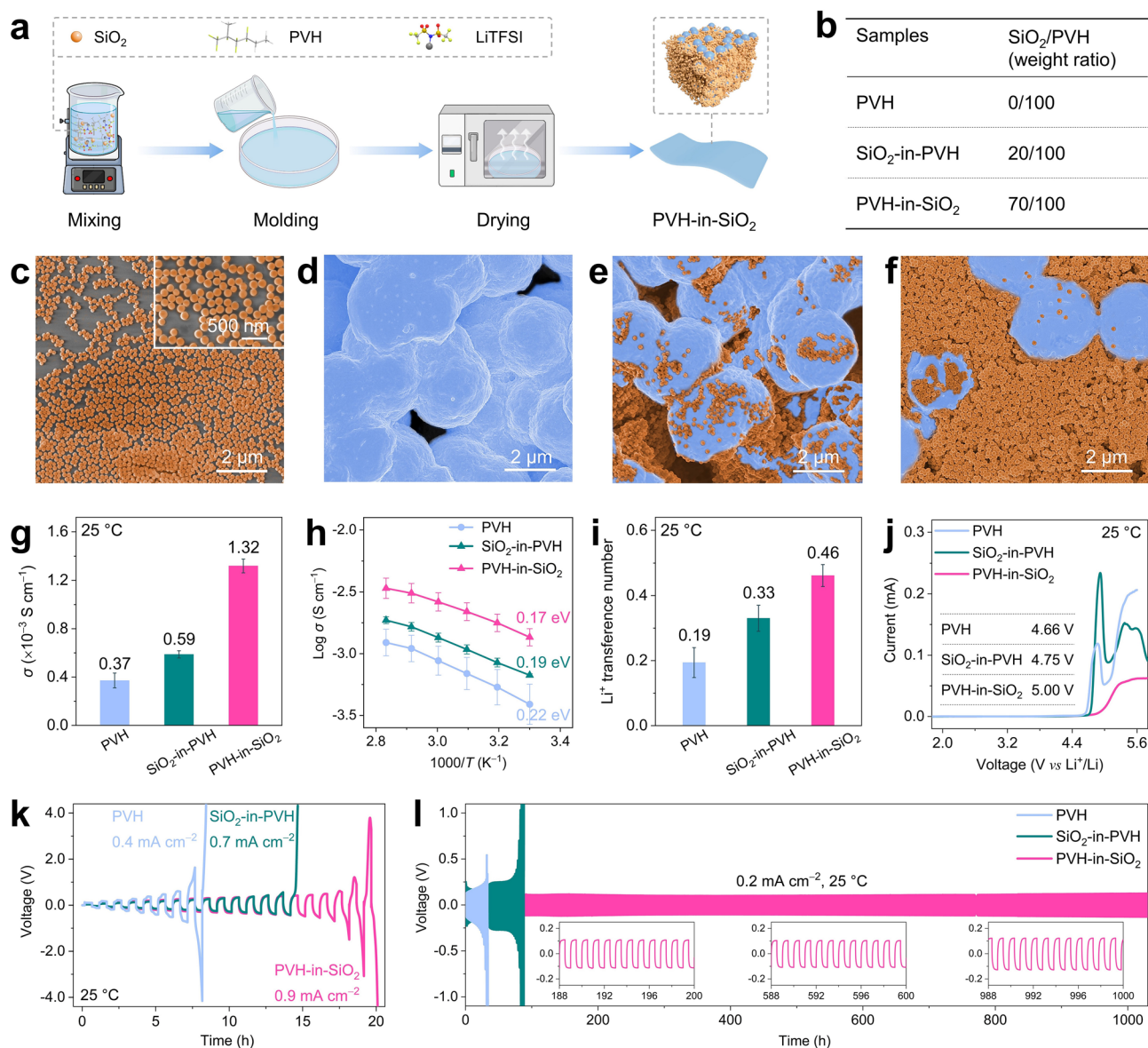
Fig. 2 Morphology, ion conduction, and electrochemical stability of PVH-in-SiO₂. **a** Schematic of the preparation process of PVH-in-SiO₂. The term LiTFSI represents lithium bis(trifluoromethanesulfonyl)imide. **b** SiO₂/PVH weight ratios for PVH, SiO₂-in-PVH, and PVH-in-SiO₂. Note that the LiTFSI/PVH ratios of all three samples were kept at 100/100 wt%. **c**, SEM images of SiO₂ nanoparticles. **d–f** Top-view SEM images of **d** PVH, **e** SiO₂-in-PVH, and **f** PVH-in-SiO₂ CSEs. The blue and orange represent the PVH spheres and SiO₂ nanoparticles, respectively. **g–i** Li⁺ conducting properties: **g** ionic conductivities (σ), **h** Arrhenius plots between σ and temperature (T), **i** Li⁺ transference numbers of PVH, SiO₂-in-PVH, and PVH-in-SiO₂ CSEs. **j–l** Electrochemical stability against Li metal anodes: **j** LSV curves, **k** CCD values (Li plating/stripping time: 0.5 h per step; current density increment: 0.05 mA cm⁻²), and **l** galvanostatic voltage profiles of Li∥Li symmetric cells at 0.2 mA cm⁻² (1 h per step) of PVH, SiO₂-in-PVH, and PVH-in-SiO₂. All measurements were carried out at 25 °C, except that the Arrhenius plots were collected from 30 to 80 °C

occurs. After introducing SiO₂ nanoparticles, the small oxidation peak disappears, and the fast oxidation voltage rises to 4.75 and 5.00 V in the cases of SiO₂-in-PVH and PVH-in-SiO₂, respectively. These findings imply that the PVH-in-SiO₂ exhibits robust electrochemical oxidation

stability (Table S3) [26, 28, 38–43, 45–48, 50, 52], showing good potential for pairing with high-voltage cathodes to realize high-energy–density solid-state Li metal batteries. We also evaluated the electrochemical stability of PVH-in-SiO₂ against Li metal anode by assembling Li∥Li symmetric

cells. Figure 2k shows the critical current density (CCD) curves, in which the PVH-in-SiO$_2$ exhibits a high CCD of 0.90 mA cm^{-2}. In contrast, the PVH and SiO$_2$-in-PVH only show a low CCD of 0.40 and 0.70 mA cm^{-2}, respectively. In addition, their long-term electrochemical stability against Li metal anode is also investigated at different current densities (Figs. 2l and S14). The PVH-in-SiO$_2$ remains stable for over 1000 h at the current densities of 0.1 and 0.2 mA cm^{-2}, with corresponding overpotentials of only 68.2 and 88.6 mV, respectively. On the contrary, the SiO$_2$-in-PVH quickly fails after 330 and 88 h at 0.1 and 0.2 mA cm^{-2}, respectively. Similar poor stability is also observed in the case of PVH (51 and 33 h at 0.1 and 0.2 mA cm^{-2}, respectively). The poor stability of PVH not only originates from the sluggish ion conduction but is also attributed to its chemical instability against Li metal anodes [44]. Quantitatively, the total Li stripping/plating capacity of PVH-in-SiO$_2$-based symmetric cells is over 200 mAh cm^{-2}, which is more competitive than those using other CSEs and PSEs (Table S3) [26, 28, 38–43, 45–48, 50, 52].

Other parameters that influence the properties of PVH-in-SiO$_2$ are also examined. For instance, if the SiO$_2$/PVH weight ratio is further increased (e.g., 100/100), it is hard to form mechanically durable CSE films (Fig. S15); if the size of SiO$_2$ nanoparticles is increased (e.g., 488 nm), the sphere morphology of PVH disappears, and ionic conductivity declines to 1.2×10^{-4} S cm^{-1} at 25 °C (Figs. S16 and S17).

To summarize, we have successfully realized an innovative PVH-in-SiO$_2$ (i.e., "polymer guest-in-ceramic host") architecture with superionic conductivity (1.32×10^{-3} S cm^{-1} at 25 °C), low activation energy (0.17 eV), and electrochemical stability by introducing 158 nm SiO$_2$ nanoparticles into the interconnected PVH spheres with a SiO$_2$/PVH weight ratio of 70/100.

2.2 Li$^+$ Transport Mechanism of PVH-in-SiO$_2$

We initially employed X-ray diffraction (XRD) to determine the crystallinity, and the XRD patterns are shown in Fig. S18. Owing to the highly disordered structure of the SiO$_2$ nanoparticles, the two primary reflections at 20.2° and 38.8° can be assigned to the crystalline domain of PVH [39]. As the SiO$_2$ nanoparticle content rises, the reflection intensity of these two peaks gradually lessens. Consequently, the PVH-in-SiO$_2$ exhibits a much lower crystallinity of 19% than PVH (28%) and SiO$_2$-in-PVH (25%), as Fig. 3a discloses.

Therefore, the PVH-in-SiO$_2$ has more amorphous regions than PVH and SiO$_2$-in-PVH, which are advantageous to fast Li$^+$ transport [55].

We subsequently utilized Raman spectroscopy to elucidate the dissociation of LiTFSI (Fig. 3b). Three peaks at 741, 744, and 749 cm^{-1} can be distinguished, corresponding to the free TFSI$^-$, contact ion pairs (CIP), and aggregated ion pairs (AGG), respectively [56]. Among them, the free TFSI$^-$ anions are formed from the dissociation of LiTFSI, while the CIP and AGG represent the TFSI$^-$ anions associated with one or more Li$^+$ cations, respectively [39]. In other words, the higher the free TFSI$^-$ content is, the higher the dissociation degree of LiTFSI is. Quantitatively, the PVH-in-SiO$_2$ has the highest free TFSI$^-$ content of 87%, which is 1.3 and 1.1 times that of PVH (67%) and SiO$_2$-in-PVH (76%), as Fig. 3c depicts. These results suggest that the PVH-in-SiO$_2$ architecture can significantly facilitate the dissociation of LiTFSI, providing more moveable Li$^+$ for enhancing ionic conductivity [57]. This conclusion is further proved by calculating the dissociation energy of LiTFSI on SiO$_2$ surface, PVH chain, and SiO$_2$/PVH interface via density functional theory (DFT) (Fig. S19). The SiO$_2$/PVH interface shows the lowest dissociation energy of 0.72 eV compared to SiO$_2$ surface (2.46 eV) and PVH chain (1.36 eV), indicating that the SiO$_2$/PVH interface can effectively promote LiTFSI dissociation.

To reveal the Li$^+$ transport channel in PVH-in-SiO$_2$, we performed solid-state nuclear magnetic resonance (SSNMR) spectroscopy by assembling ^{6}Li symmetric cells using PVH-in-SiO$_2$ as CSEs. The ^{6}Li symmetric cells were cycled at a stripping/plating current of 50 μA for 10 cycles (Fig. S20), upon which a portion of ^{7}Li$^+$ in the PVH-in-SiO$_2$ was replaced by ^{6}Li$^+$. We observe that the pristine PVH-in-SiO$_2$ exhibits a ^{6}Li resonance at *ca.* 0.02 ppm, which shifts to *ca.* -0.02 ppm after cycling tests (Fig. 3d), indicating the change of ^{6}Li$^+$ chemical environments [58]. More specifically, the resonance peak can be further fitted into two peaks at approximately 0.02 ppm and -0.03 ppm. The former peak (0.02 ppm) belongs to the ^{6}Li$^+$ in the PVH, while the latter one (-0.03 ppm) represents the ^{6}Li$^+$ at the SiO$_2$/PVH interfaces (see details in Fig. S21). Quantitatively, the ^{6}Li$^+$ ratio in the PVH shows a tremendous decline from 98% to 47% after cycling, corresponding to a dramatical increase of the ^{6}Li$^+$ ratio at the SiO$_2$/PVH interfaces from 2% to 53% (Fig. 3e). These SSNMR results suggest that the Li$^+$ in the PVH-in-SiO$_2$ has a strong tendency to migrate from the
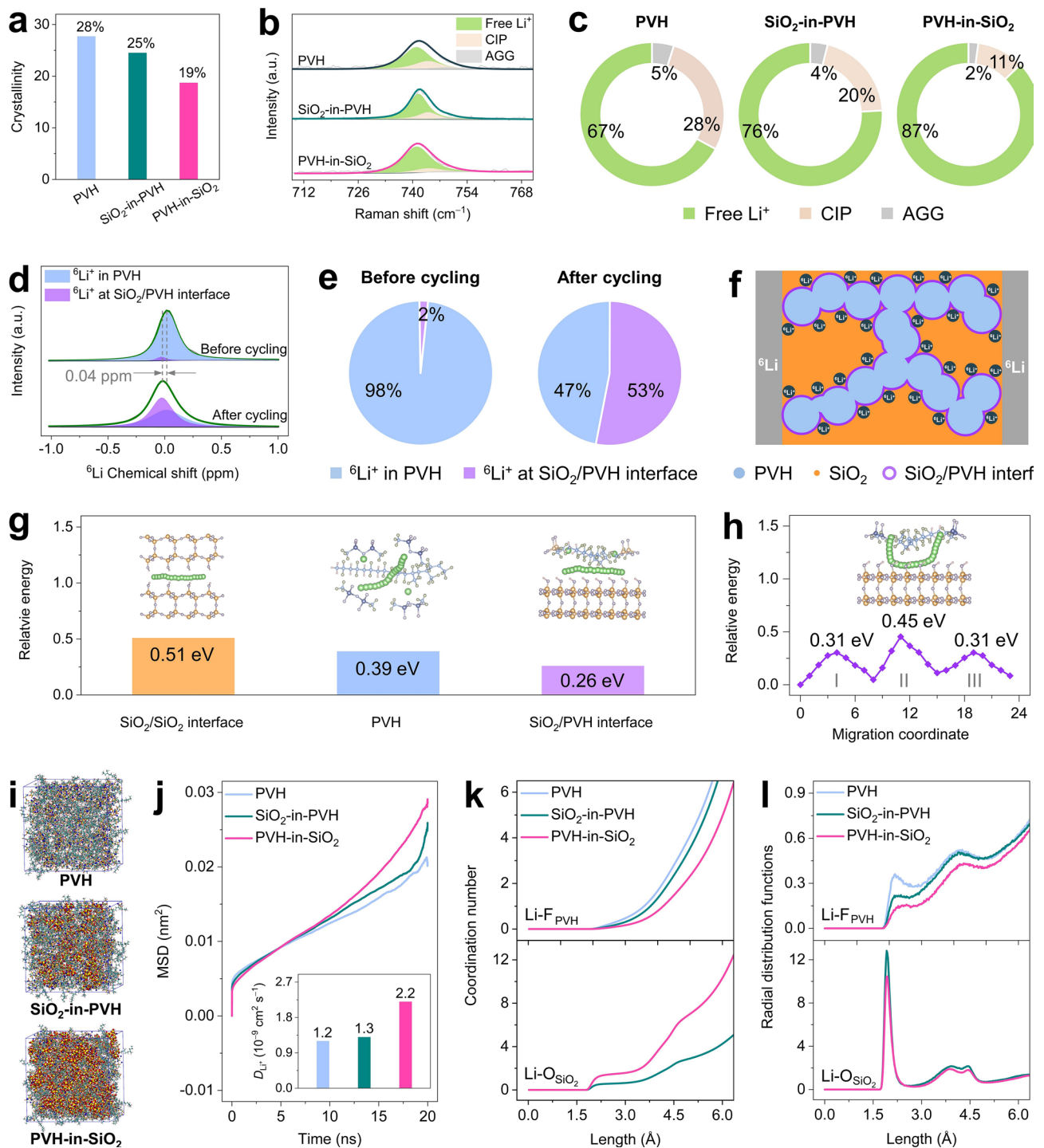
Fig. 3 Li⁺ transport mechanism of PVH-in-SiO₂. **a–c** Structural and spectral analyses of PVH, SiO₂-in-PVH, and PVH-in-SiO₂: **a** crystallinity, **b** Raman spectra, and **c** ratios of free TFSI⁻, CIP, and AGG. **d** ⁶Li SSNMR spectra of PVH-in-SiO₂ before and after plating/stripping. **e** Quantification results of ⁶Li⁺ amount in the PVH and at the SiO₂/PVH interfaces of PVH-in-SiO₂ before and after plating/stripping. **f** Schematic of ⁶Li⁺ migration and transport in PVH-in-SiO₂. **g** Calculation models (insets) and energy barriers of Li⁺ transport along the SiO₂/SiO₂ interfaces, PVH chains, and SiO₂/PVH interfaces. **h** Calculation models (inset) and energy barriers of dynamic Li⁺ migration process from PVH to SiO₂ and back to PVH (Stage I, II, and III). **i–l** MD simulation results of PVH, SiO₂-in-PVH, and PVH-in-SiO₂: **i** Model snapshots, **j** MSD curves, **k** coordination numbers, and **l** radial distribution functions

PVH to the SiO_2/PVH interfaces and subsequently transports at the SiO_2/PVH interfaces upon in-service operation, as Fig. 3f illustrates.

We conducted DFT calculations to elucidate why Li^+ tends to migrate to and transport at the SiO_2/PVH interfaces in the case of PVH-in-SiO_2. Generally, there are three routes for Li^+ transport, including SiO_2/SiO_2 interfaces, PVH chains, and SiO_2/PVH interfaces (insets of Fig. 3g). On the one hand, the Li^+ transport at the SiO_2/SiO_2 interfaces has the highest energy barrier of 0.51 eV (Fig. 3g), suggesting that the SiO_2/SiO_2 interfaces are thermodynamically unfavorable for Li^+ transport. This finding is in good agreement with the SSNMR results that no $^6Li^+$ peak at the SiO_2/SiO_2 interfaces is found. On the other hand, the energy barriers of Li^+ transport along the PVH chain and at the SiO_2/PVH interfaces are significantly reduced to 0.39 and 0.26 eV, respectively, indicating that SiO_2/PVH interfaces are the most energetic route for Li^+ transport. We further model the dynamic Li^+ migration process from PVH to SiO_2 and then back to PVH. In detail, this process involves three steps (inset of Fig. 3h): Li^+ migration from the PVH chain to the SiO_2 surface (Stage I), Li^+ transport along the SiO_2 surface (Stage II), and Li^+ migration from the SiO_2 surface to the PVH chain (Stage III). Figure 3h showcases that the energy barriers of Step I and Step III (0.31 eV) are much lower than that of Step II (0.45 eV). In addition, they are also lower than that of Li^+ transport along the PVH chain (0.39 eV, Fig. 3g). These results demonstrate that Li^+ in the PVH thermodynamically tends to migrate to the SiO_2/PVH interfaces and transport along the continuous interfacial highways constructed by the PVH-in-SiO_2 architecture.

In addition to the atomic scale DFT calculations, we further utilized molecular dynamics (MD) simulations to disclose the Li^+ transport behavior in PVH-in-SiO_2 on a larger scale. Figure 3i presents the snapshots of MD simulation models of PVH, SiO_2-in-PVH, and PVH-in-SiO_2, which have volumes of 207, 225, and 278 nm^3, respectively. The mean squared displacements (MSD) curves of these three samples were simulated and displayed in Fig. 3j. The MSD curve becomes steeper as more SiO_2 nanoparticles are introduced. Quantitatively, we can calculate the corresponding Li^+ diffusion coefficient (D_{Li^+}) from MSD curves because it is proportional to the curve slope. (Time range between 10 and 18 ns is used.) The PVH exhibits a low D_{Li^+} of 1.2×10^{-9} cm^2 s^{-1}, which nearly doubles in the case of PVH-in-SiO_2 (2.2×10^{-9} cm^2 s^{-1}, inset of Fig. 3j),

demonstrating that the PVH-in-SiO_2 has a much better Li^+ transport kinetics than PVH and SiO_2-in-PVH. In addition, the coordination environment of Li^+ was analyzed to demonstrate its transport at the SiO_2/PVH interfaces. Figure 3k shows the coordination numbers between Li^+ and F atoms of PVH (labeled as Li-F_{PVH}) and between Li^+ and O atoms of SiO_2 (labeled as Li-O_{SiO_2}). As the SiO_2 content increases, the coordination numbers of Li-F_{PVH} decreases, while the coordination numbers of Li-O_{SiO_2} increases. These results suggest that Li^+ is favorable to migrating to the SiO_2/PVH interfaces, which is further validated by the radial distribution functions (Fig. 3l). For instance, the dominant peak of Li-F_{PVH} of PVH-in-SiO_2 locates at 2.54 Å, which is higher than those of PVH (2.18 Å) and SiO_2-in-PVH (2.36 Å). The peak shift to longer distances can be attributed to the Li^+ migration to the SiO_2/PVH interfaces.

Finally, we conduct the finite element analysis to simulate ion transport in a PVH-in-SiO_2 model with a simulation calculation area of 18 μm × 18 μm (Fig. S22a), further revealing the impact of SiO2/PVH interfaces on Li^+ transport. Figure S22b is the distribution of current densities in the PVH-in-SiO_2 model. The SiO_2/PVH interface exhibits a high current density of 10^2–10^3 mA cm^{-2}, whereas the current density in PVH is less than 10^2 mA cm^{-2}. This result suggests that the SiO_2/PVH interface provides highways for ion transport and plays a dominant role in the ion transport process.

To summarize, the PVH-in-SiO_2 architecture significantly decreases the crystallinity of the PVH guest, providing sufficient amorphous areas for more accessible Li^+ transport in the PVH. In addition, the PVH-in-SiO_2 architecture also facilitates the dissociation of LiTFSI, achieving high-concentration free Li^+. These Li^+ cations are thermodynamically and kinetically favorable to migrate to and transport at the continuous SiO_2/PVH interfaces because of their low energy barriers and high diffusion coefficient, resulting in the superionic properties of PVH-in-SiO_2.

2.3 Performance of Solid-State Full Cells Based on PVH-in-SiO_2

We first assembled solid-state full cells using $LiFePO_4$ (LFP), PVH-in-SiO_2, and Li metal as cathode, solid-state electrolyte, and anode, respectively (Fig. 4a). The mass loading of LFP is 1.5–2.5 mg cm^{-2}. The rate performance was evaluated at various current densities under 25 °C (Figs. 4b

and S23). The LFP|PVH-in-SiO$_2$|Li full cells show high reversible specific capacities of 157.4, 154.5, 148.1, 139.6, and 126.0 mAh g^{-1} at 0.1C, 0.2C, 0.5C, 1C, and 2C, respectively. When the current density soars to 5C, a high specific capacity of 75.6 mAh g^{-1} is also achieved, which can immediately return to 152.6 mAh g^{-1} once the current density recovers to 0.1C. In contrast, the LFP|SiO$_2$-in-PVH|Li full cells showcase much lower specific capacities at high current densities (e.g., only 27.4 mAh g^{-1} is delivered at 5C), despite that they have good specific capacities at small current densities (< 0.5C). In the case of LFP|PVH|Li, even worse performance is delivered at all current densities. These findings demonstrate that the PVH-in-SiO$_2$ exhibits excellent rate capability, especially at high current densities, which can be further verified by the polarization voltage result (Figs. 4c and S24). For instance, the polarization voltage of LFP|PVH-in-SiO$_2$|Li at 2C is approximately 0.51 V, which is only 65% and 66% of those of LFP|PVH|Li (0.78 V) and LFP|SiO$_2$-in-PVH|Li (0.77 V).

The cycling performances of LFP|PVH-in-SiO$_2$|Li full cells were also evaluated under 25 °C, as Fig. 4d shows. When the current density is fixed at 0.2C, the LFP|PVH-in-SiO$_2$|Li delivers a high initial specific capacity of 152.8 mAh g^{-1}, which gradually increases to 158.6 mAh g^{-1} after 20 cycles. The specific capacity increase is mainly attributed to the activation of LFP and the interface stabilization between electrodes and PVH-in-SiO$_2$ [59, 60]. The specific capacity remains stable in the following cycles, and an outstanding capacity retention of 99.4% is obtained after 100 cycles. In addition, the LFP|PVH-in-SiO$_2$|Li also exhibits a high average Coulombic efficiency of 99.8% upon cycling, indicating the excellent cyclability of PVH-in-SiO$_2$. In contrast, both LFP|SiO$_2$-in-PVH|Li and LFP|PVH|Li show poor cycling stability. The specific capacity of LFP|SiO$_2$-in-PVH|Li quickly falls after 80 cycles, while the LFP|PVH|Li experiences abnormal discharging/charging behaviors after only 10 cycles and fails at the 20th cycle (Fig. S25). We further evaluated the long-term cyclability at a higher current density of 3C under 25 °C. The LFP|PVH-in-SiO$_2$|Li delivers a high capacity retention of 92.9% after 300 cycles, whereas the LFP|SiO$_2$-in-PVH|Li and LFP|PVH|Li only achieve a poor capacity retention of 42.1% (Fig. 4e). Furthermore, when we raise the current density to 5C, the LFP|PVH-in-SiO$_2$|Li can still have an attractive capacity retention of 77.5% after 300 cycles at 25 °C (Fig. S26). Even compared to recently reported solid-state LFP|Li full cells,

our LFP|PVH-in-SiO$_2$|Li also shows overwhelming cycling stability, especially at high current densities (Fig. 4f and Table S4) [27, 31, 43, 47, 52, 61–73].

High-mass-loading LFP cathodes were also employed to demonstrate the potential of PVH-in-SiO$_2$ in practical applications. Figure 4g shows the cycling performance of solid-state LFP|PVH-in-SiO$_2$|Li full cells with a high mass loading of 9.2 mg cm^{-2} under 25 °C. An impressive specific capacity of 136.0 mAh g^{-1} is delivered at the current density of 0.2C after 100 cycles, corresponding to a superior capacity retention of 92.4%. In contrast, the LFP|SiO$_2$-in-PVH|Li and LFP|PVH|Li full cells quickly fail after 5 and 3 cycles (Fig. S27). These findings verify that the PVH-in-SiO$_2$ is promising for practical solid-state Li metal battery applications. In addition to the LFP cathode, we also employ LiNi$_{0.6}$Co$_{0.2}$Mn$_{0.2}$O$_2$ (labeled as NCM622) as a typical nickel-rich oxide cathode in order to investigate the compatibility of PVH-in-SiO$_2$ with high-voltage cathode materials, as Fig. 4h displays. The resulted solid-state NCM622|PVH-in-SiO$_2$|Li full cells exhibit a high initial specific capacity of 145.6 mAh g^{-1}, which even slightly increases to 147.1 mAh g^{-1} after 100 cycles at the current density of 0.2C under 25 °C. On the contrary, the NCM622|SiO$_2$-in-PVH|Li and NCM622|PVH|Li full cells quickly deteriorate in the initial several cycles and only deliver small specific capacities of 62.3 and 26.1 mAh g^{-1}, respectively, after 50 cycles. These results suggest that the PVH-in-SiO$_2$ holds excellent potential for high-energy–density solid-state Li metal batteries.

We also assembled LFP|PVH-in-SiO$_2$|Li pouch cells with a lateral size of 3.5×4.0 cm^2 to demonstrate the potential applications of our PVH-in-SiO$_2$ for multipurpose solid-state batteries (Fig. 4i). The pouch cells can power 36 light-emitting diode (LED) bulbs under the flat state. When folded and unfolded in sequence, the pouch cells can still power the LED bulbs, implying that the PVH-in-SiO$_2$ promises flexible solid-state Li metal batteries. Moreover, the pouch cells can still work properly without fuming or burning when they are cut into several small pieces, demonstrating their high safety under extremely harsh conditions.
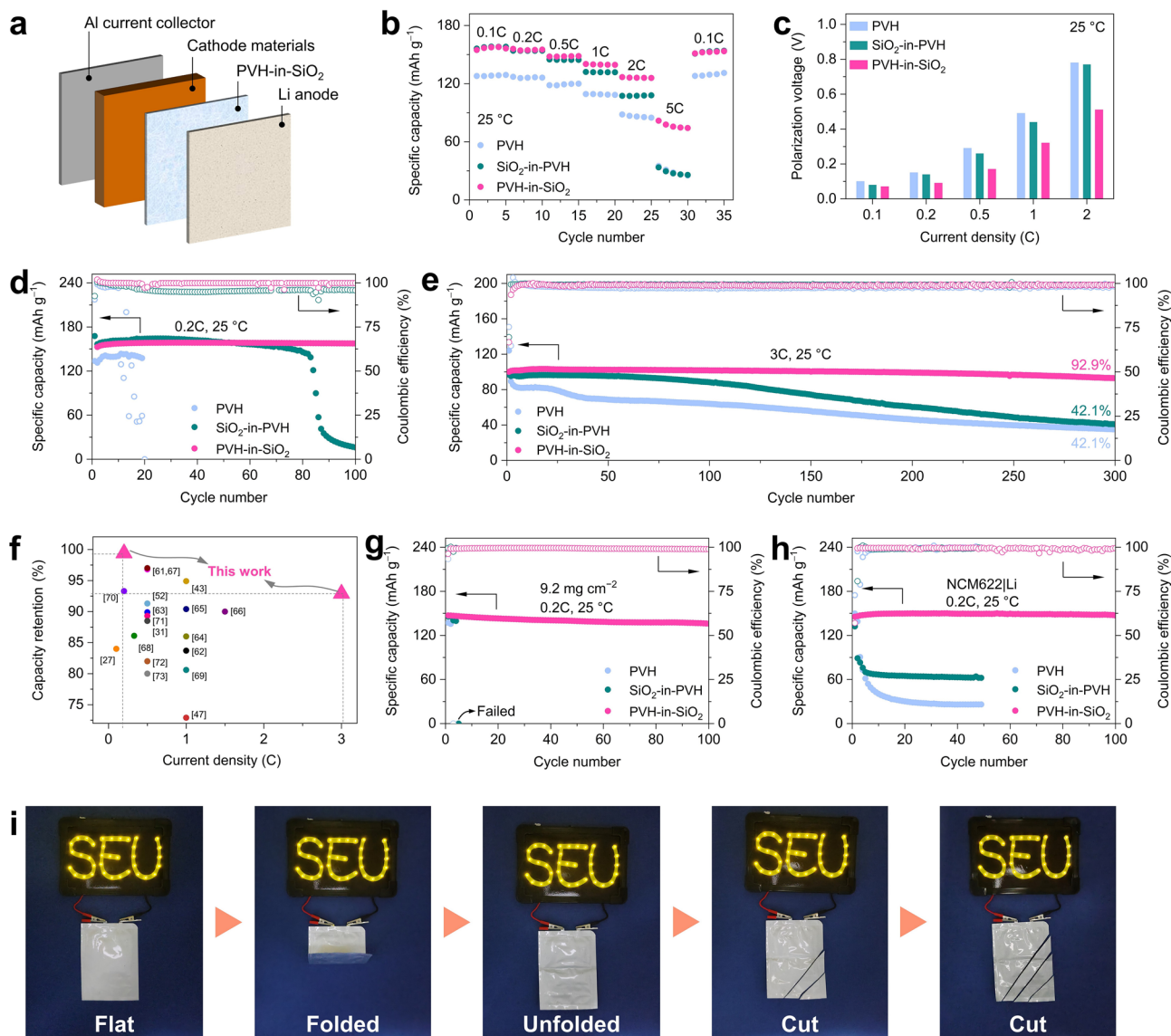
Fig. 4 Electrochemical performance of solid-state full cells. **a** Schematic of the PVH-in-SiO$_2$-based solid-state full cells. **b, c** Rate capability of LFP|PVH|Li, LFP|SiO$_2$-in-PVH|Li, and LFP|PVH-in-SiO$_2$|Li at 25 °C: **b** specific capacity and **c** corresponding polarization voltage at various current densities. The polarizations of LFP|PVH|Li and LFP|SiO$_2$-in-PVH|Li at 5C are too large to determine their polarization voltages (Supplementary Fig. S17). **d, e** Cycling stability of LFP|PVH|Li, LFP|SiO$_2$-in-PVH|Li, and LFP|PVH-in-SiO$_2$|Li at the current density of **d** 0.2C and **e** 3.0C under 25 °C. **f** Comparison of specific capacity retention of LFP|PVH-in-SiO$_2$|Li with recently reported solid-state LFP|Li batteries using polymer solid electrolytes. **g** Cycling performance of LFP|PVH-in-SiO$_2$|Li at high mass loadings of 9.2 mg cm^{-2} under 25 °C (current density: 0.2C). **h** Cycling performance of NCM622|PVH-in-SiO$_2$|Li at the current density of 0.2C under 25 °C. **i** Digital photographs of LED bulbs powered by LFP|PVH-in-SiO$_2$|Li pouch cells under different states and conditions: flat, folded, unfolded, and cut

2.4 Versatility of Host–Guest Inversion Engineering Strategy

The outstanding properties and performance of PVH-in-SiO$_2$ for Li$^+$ conduction and solid-state Li metal batteries motivate us to explore the feasibility of host–guest inversion engineering in solid-state Na and K metal batteries, which are promising for grid-scale energy storage because of their low costs and relatively high energy densities [74–76]. PVH-in-SiO$_2$-Na and PVH-in-SiO$_2$-K are obtained by simply replacing LiTFSI with NaTFSI and KTFSI, respectively, with other preparation parameters unchanged. Figure 5a

depicts the SEM images of PVH-Na and PVH-in-SiO$_2$-Na. The PVH also forms interconnected spheres, which are also densely covered by SiO$_2$ nanoparticles. As a result, the PVH-in-SiO$_2$-Na exhibits a high ionic conductivity of 3.03×10^{-4} S cm^{-1} at 25 °C, which is almost 14 times that of PVH-Na (2.2×10^{-5} S cm^{-1}, Figs. 5b and S28). In addition, PVH-in-SiO$_2$-Na also shows a low activation energy of 0.30 eV, significantly smaller than that of PVH-Na (0.52 eV, inset of Figs. 5b and S29). Similar results are also observed in the case of PVH-K and PVH-in-SiO$_2$-K (Fig. 5c). Specifically, the PVH-in-SiO$_2$-K exhibits a high ionic conductivity of 2.56×10^{-4} S cm^{-1} at 25 °C, which is 64 times that of PVH -K (4.0×10^{-6} S cm^{-1}, Figs. 5d and S30). In addition, the PVH-in-SiO$_2$-K also delivers a low activation energy of 0.31 eV (inset of Fig. 5d), whereas we cannot

obtain reliable activation energy for PVH-K owing to their extremely low ionic conductivities and abnormal EIS curves (Figs. S31 and S32). These findings once again demonstrate that the host–guest inversion engineering strategy is a versatile approach to significantly facilitating ion transport for achieving high room-temperature ionic conductivity.

To evaluate the implementations of PVH-in-SiO$_2$-Na and PVH-in-SiO$_2$-K, solid-state full cells were assembled using Na$_3$V$_2$(PO$_4$)$_3$ (NVP) and potassium Prussian blue (KPB) as cathode materials, respectively. In the case of NVP|PVH-in-SiO$_2$-Na|Na (Fig. 5e), high specific capacities of 108.1, 103.1, 97.3, and 93.7 mAh g^{-1} are delivered at the current density of 0.1C, 0.2C, 0.5C, and 1C under 25 °C, respectively. Even when the current density is further increased to 2C, a large specific capacity of 78.4 mAh g^{-1} is retained,
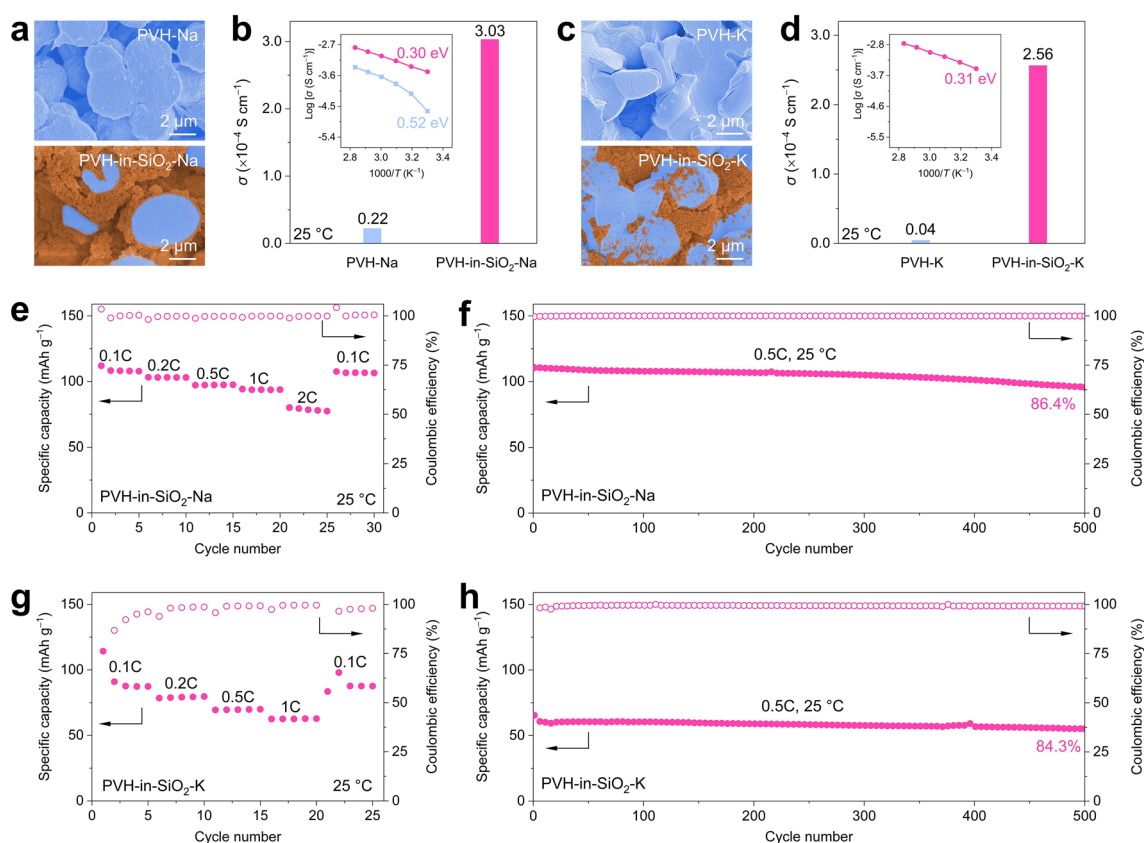
Fig. 5 Morphologies, ion-conducting properties, and full-cell performance of PVH-in-SiO$_2$-Na and PVH-in-SiO$_2$-K. **a** SEM images of PVH-Na and PVH-in-SiO$_2$-Na. **b** Ionic conductivities at 25 °C and activation energies (inset) of PVH-Na and PVH-in-SiO$_2$-Na. **c** SEM images of PVH-K and PVH-in-SiO$_2$-K. **d** Ionic conductivities at 25 °C and activation energies (inset) of PVH-K and PVH-in-SiO$_2$-K. Note that the activation energy of PVH-K cannot be calculated (details in Supplementary information). **e, f** Electrochemical performance of NVP|PVH-Na|Na and NVP|PVH-in-SiO$_2$-Na|Na full cells at 25 °C: **e** rate capability at various current densities and **f** cycling stability at 0.5C. **g, h** Electrochemical performance of KPB|PVH-K|K and KPB|PVH-in-SiO$_2$-K|K full cells at 25 °C: **g** rate capability at various current densities and **h** cycling stability at 0.5C

demonstrating the remarkable rate capability of the PVH-in-SiO$_2$-Na. The cycling stability of NVP|PVH-in-SiO$_2$-Na|Na was assessed at the current density of 0.5C under 25 °C (Fig. 5f). An excellent specific capacity of 95.5 mAh g^{-1} is achieved after 500 cycles, corresponding to a capacity retention of as high as 86.4%. Furthermore, the average Coulombic efficiency upon cycling exceeds 99.9%, indicating the superb cyclability of PVH-in-SiO$_2$-Na. On the contrary, the NVP|PVH-Na|Na full cells quickly fail after several cycles, verifying their inferior rate and cycling performance (Figs. S33 and S34). Similar results are also observed in the cases of PVH-in-SiO$_2$-K and PVH-K (Fig. 5g, h). The KPB|PVH-in-SiO$_2$-K|K delivers fantastic rate capability (87.7 and 62.6 mAh g^{-1} at 0.1C and 1C, respectively) and cycling performance (84.3% capacity retention after 500 cycles at 0.5C) under 25 °C. In contrast, the KPB|PVH-K|K cannot work at all. These electrochemical performance results undoubtedly confirm the versatility and superiority of our host–guest inversion engineering strategy, making it promising for next-generation, advanced solid-state alkali metal batteries.

3 Conclusions

We have successfully realized a superionic CSE using SiO$_2$ nanoparticles as cost-effective passive ceramic hosts and the interconnected PVH spheres as polymer guests, forming an innovative "PVH-in-SiO$_2$" (i.e., "polymer guest-in-ceramic host") architecture with optimized and continuous SiO$_2$/PVH interfacial contacts. The PVH-in-SiO$_2$ architecture not only significantly inhibits the crystallization of PVH to offer sufficient amorphous areas for Li$^+$ transport, but also greatly facilitates the dissociation of LiTFSI to achieve high-concentration moveable Li$^+$. Owing to the low diffusion energy barriers and high diffusion coefficient, these moveable Li$^+$ are thermodynamically and kinetically favorable to migrate to and transport at the continuous SiO$_2$/PVH interfaces. Therefore, the PVH-in-SiO$_2$ exhibits an overwhelmingly high ionic conductivity of 1.32×10^{-3} S cm^{-1} at 25 °C, with an ultralow residual solvent content of 2.9 wt%. The PVH-in-SiO$_2$ also shows outstanding electrochemical stability with Li metal anode and various cathode materials. As a result, the LFP|PVH-in-SiO$_2$|Li full cells deliver excellent rate capability and cyclability at high current rates (92.9% and 77.5% capacity retentions at 3C and 5C after 300 cycles under 25 °C, respectively). In addition, the PVH-in-SiO$_2$

showcases good compatibility with high-mass-loading cathodes and high-capacity NCM622, demonstrating good cycling and safety performance. More significantly, the versatility of our host–guest inversion engineering strategy is verified by constructing advanced PVH-in-SiO$_2$-Na and PVH-in-SiO$_2$-K by simply replacing LiTFSI with NaTFSI and KTFSI, respectively. The PVH-in-SiO$_2$-Na and PVH-in-SiO$_2$-K not only have high ionic conductivities at 25 °C (both are in the order 10^{-4} S cm^{-1}) but also exhibit excellent full-cell performance. Our host–guest inversion engineering strategy offers a simple and large-scale approach to fabricating superionic CSEs with high-throughput Li$^+$ transport and low costs, paving an avenue for the practical application of next-generation solid-state Li metal batteries and beyond.

Author Contributions Xiong Xiong Liu: Investigation, data analysis, original draft writing. Long Pan: Conceptualization, manuscript revision, supervision, funding. Haotian Zhang, Pengcheng Yuan, Mufan Cao, Yaping Wang, Zeyuan Xu, Min Gao: data analysis. ZhengMing Sun: Conceptualization, review, supervision.

Declarations

References

1. Q. Zhao, S. Stalin, C.-Z. Zhao, L.A. Archer, Designing solid-state electrolytes for safe, energy-dense batteries. Nat. Rev. Mater. **5**, 229–252 (2020). https://doi.org/10.1038/s41578-019-0165-5

2. X. Hu, Z. Zhang, X. Zhang, Y. Wang, X. Yang et al., External-pressure–electrochemistry coupling in solid-state lithium metal batteries. Nat. Rev. Mater. **9**, 305–320 (2024). https://doi.org/10.1038/s41578-024-00669-y

3. X. Zhang, S. Cheng, C. Fu, G. Yin, L. Wang et al., Advancements and challenges in organic–inorganic composite solid electrolytes for all-solid-state lithium batteries. Nano-Micro Lett. **17**, 2 (2024). https://doi.org/10.1007/s40820-024-01498-y

4. D. Wu, L. Chen, H. Li, F. Wu, Solid-state lithium batteries-from fundamental research to industrial progress. Prog. Mater. Sci. **139**, 101182 (2023). https://doi.org/10.1016/j.pmatsci.2023.101182

5. C. Yang, Q. Wu, W. Xie, X. Zhang, A. Brozena et al., Copper-coordinated cellulose ion conductors for solid-state batteries. Nature **598**, 590–596 (2021). https://doi.org/10.1038/s41586-021-03885-6

6. Z. Zhang, W.-Q. Han, From liquid to solid-state lithium metal batteries: fundamental issues and recent developments. Nano-Micro Lett. **16**, 24 (2023). https://doi.org/10.1007/s40820-023-01234-y

7. Y. Liu, J. Wang, Y. Shao, R. Deng, J. Zhu et al., Recent advances in scalable synthesis and performance of Janus polymer/inorganic nanocomposites. Prog. Mater. Sci. **124**, 100888 (2022). https://doi.org/10.1016/j.pmatsci.2021.100888

8. L.-Z. Fan, H. He, C.-W. Nan, Tailoring inorganic–polymer composites for the mass production of solid-state batteries. Nat. Rev. Mater. **6**, 1003–1019 (2021). https://doi.org/10.1038/s41578-021-00320-0

9. S. Pazhaniswamy, S.A. Joshi, H. Hou, A.K. Parameswaran, S. Agarwal, Hybrid polymer electrolyte encased cathode particles interface-based core–shell structure for high-performance room temperature all-solid-state batteries. Adv. Energy Mater. **13**, 2202981 (2023). https://doi.org/10.1002/aenm.202202981

10. S. Liu, Y. Zhao, X. Li, J. Yu, J. Yan et al., Solid-state lithium metal batteries with extended cycling enabled by dynamic adaptive solid-state interfaces. Adv. Mater. **33**, e2008084 (2021). https://doi.org/10.1002/adma.202008084

11. C. Bao, C. Zheng, M. Wu, Y. Zhang, J. Jin et al., 12 μm-thick sintered garnet ceramic skeleton enabling high-energy-density solid-state lithium metal batteries. Adv. Energy Mater. **13**, 2204028 (2023). https://doi.org/10.1002/aenm.202204028

12. J. Zheng, M. Tang, Y.-Y. Hu, Lithium ion pathway within $Li_7La_3Zr_2O_{12}$-polyethylene oxide composite electrolytes.

13. C. Bao, C. Zheng, J. Zhang, Y. Zhang, Z. You et al., A high performance fireproof quasi-solid-state electrolyte enabled by multi-phase synergistic mechanism. Energy Storage Mater. **68**, 103362 (2024). https://doi.org/10.1016/j.ensm.2024.103362

14. Y. Wang, J. Ju, S. Dong, Y. Yan, F. Jiang et al., Facile design of sulfide-based all solid-state lithium metal battery: *in situ* polymerization within self-supported porous argyrodite skeleton. Adv. Funct. Mater. **31**, 2101523 (2021). https://doi.org/10.1002/adfm.202101523

15. Y. Su, X. Zhang, C. Du, Y. Luo, J. Chen et al., An all-solid-state battery based on sulfide and PEO composite electrolyte. Small **18**, e2202069 (2022). https://doi.org/10.1002/smll.202202069

16. L. Pan, S. Sun, G. Yu, X.X. Liu, S. Feng et al., Stabilizing solid electrolyte/Li interface *via* polymer-in-salt artificial protection layer for high-rate and stable lithium metal batteries. Chem. Eng. J. **449**, 137682 (2022). https://doi.org/10.1016/j.cej.2022.137682

17. W. Zha, W. Li, Y. Ruan, J. Wang, Z. Wen, In situ fabricated ceramic/polymer hybrid electrolyte with vertically aligned structure for solid-state lithium batteries. Energy Storage Mater. **36**, 171–178 (2021). https://doi.org/10.1016/j.ensm.2020.12.028

18. J. Janek, W.G. Zeier, Challenges in speeding up solid-state battery development. Nat. Energy **8**, 230–240 (2023). https://doi.org/10.1038/s41560-023-01208-9

19. O. Sheng, C. Jin, T. Yang, Z. Ju, J. Luo et al., Designing biomass-integrated solid polymer electrolytes for safe and energy-dense lithium metal batteries. Energy Environ. Sci. **16**, 2804–2824 (2023). https://doi.org/10.1039/D3EE01173A

20. X. Yang, J. Liu, N. Pei, Z. Chen, R. Li et al., The critical role of fillers in composite polymer electrolytes for lithium battery. Nano-Micro Lett. **15**, 74 (2023). https://doi.org/10.1007/s40820-023-01051-3

21. R. Schmuch, R. Wagner, G. Hörpel, T. Placke, M. Winter, Performance and cost of materials for lithium-based rechargeable automotive batteries. Nat. Energy **3**, 267–278 (2018). https://doi.org/10.1038/s41560-018-0107-2

22. J. Schnell, F. Tietz, C. Singer, A. Hofer, N. Billot et al., Prospects of production technologies and manufacturing costs of oxide-based all-solid-state lithium batteries. Energy Environ. Sci. **12**, 1818–1833 (2019). https://doi.org/10.1039/C8EE02692K

23. K. Yang, L. Zhao, X. An, L. Chen, J. Ma et al., Determining the role of ion transport throughput in solid-state lithium batteries. Angew. Chem. Int. Ed. **62**, e202302586 (2023). https://doi.org/10.1002/anie.202302586

24. W. Yu, N. Deng, D. Shi, L. Gao, B. Cheng et al., One-dimensional oxide nanostructures possessing reactive surface defects enabled a lithium-rich region and high-voltage stability for all-solid-state composite electrolytes. ACS Nano **17**, 22872–22884 (2023). https://doi.org/10.1021/acsnano.3c07754

25. S. Liu, W. Liu, D. Ba, Y. Zhao, Y. Ye et al., Filler-integrated composite polymer electrolyte for solid-state lithium batteries.

Angew. Chem. Int. Ed. **55**, 12538–12542 (2016). https://doi.org/10.1002/anie.201607539

Adv. Mater. **35**, e2110423 (2023). https://doi.org/10.1002/adma.202110423

26. X. An, Y. Liu, K. Yang, J. Mi, J. Ma et al., Dielectric filler-induced hybrid interphase enabling robust solid-state Li metal batteries at high areal capacity. Adv. Mater. **36**, e2311195 (2024). https://doi.org/10.1002/adma.202311195

27. F. Tao, X. Wang, S. Jin, L. Tian, Z. Liu et al., A composite of hierarchical porous MOFs and halloysite nanotubes as single-ion-conducting electrolyte toward high-performance solid-state lithium-ion batteries. Adv. Mater. **35**, e2300687 (2023). https://doi.org/10.1002/adma.202300687

28. S. Lv, X. He, Z. Ji, S. Yang, L. Feng et al., A supertough and highly-conductive nano-dipole doped composite polymer electrolyte with hybrid Li$^+$-solvation microenvironment for lithium metal batteries. Adv. Energy Mater. **13**, 2302711 (2023). https://doi.org/10.1002/aenm.202302711

29. H. Liang, L. Wang, A. Wang, Y. Song, Y. Wu et al., Tailoring practically accessible polymer/inorganic composite electrolytes for all-solid-state lithium metal batteries: a review. Nano-Micro Lett. **15**, 42 (2023). https://doi.org/10.1007/s40820-022-00996-1

30. W. Liu, S.W. Lee, D. Lin, F. Shi, S. Wang et al., Enhancing ionic conductivity in composite polymer electrolytes with well-aligned ceramic nanowires. Nat. Energy **2**, 17035 (2017). https://doi.org/10.1038/nenergy.2017.35

31. L. Zhu, J. Chen, Y. Wang, W. Feng, Y. Zhu et al., Tunneling interpenetrative lithium ion conduction channels in polymer-in-ceramic composite solid electrolytes. J. Am. Chem. Soc. **146**, 6591–6603 (2024). https://doi.org/10.1021/jacs.3c11988

32. H. Huo, Y. Chen, J. Luo, X. Yang, X. Guo et al., Rational design of hierarchical "ceramic-in-polymer" and "polymer-in-ceramic" electrolytes for dendrite-free solid-state batteries. Adv. Energy Mater. **9**, 1804004 (2019). https://doi.org/10.1002/aenm.201804004

33. Z. Li, F. Liu, S. Chen, F. Zhai, Y. Li et al., Single Li ion conducting solid-state polymer electrolytes based on carbon quantum dots for Li-metal batteries. Nano Energy **82**, 105698 (2021). https://doi.org/10.1016/j.nanoen.2020.105698

34. Z. Zhang, S. Zhang, S. Geng, S. Zhou, Z. Hu et al., Agglomeration-free composite solid electrolyte and enhanced cathode-electrolyte interphase kinetics for all-solid-state lithium metal batteries. Energy Storage Mater. **51**, 19–28 (2022). https://doi.org/10.1016/j.ensm.2022.06.025

35. Y. Jin, X. Zong, X. Zhang, Z. Jia, H. Xie et al., Constructing 3D Li$^+$percolated transport network in composite polymer electrolytes for rechargeable quasi-solid-state lithium batteries. Energy Storage Mater. **49**, 433–444 (2022). https://doi.org/10.1016/j.ensm.2022.04.035

36. J. Yu, G. Zhou, Y. Li, Y. Wang, D. Chen et al., Improving room-temperature Li-metal battery performance by in situ creation of fast Li$^+$ transport pathways in a polymer-ceramic electrolyte. Small **19**, e2302691 (2023). https://doi.org/10.1002/smll.202302691

37. S. Zhou, S. Zhong, Y. Dong, Z. Liu, L. Dong et al., Composition and structure design of poly(vinylidene fluoride)-based solid polymer electrolytes for lithium batteries. Adv. Funct.

Mater. **33**, 2214432 (2023). https://doi.org/10.1002/adfm.202214432

38. X. Zhang, S. Wang, C. Xue, C. Xin, Y. Lin et al., Self-suppression of lithium dendrite in all-solid-state lithium metal batteries with poly(vinylidene difluoride)-based solid electrolytes. Adv. Mater. **31**, e1806082 (2019). https://doi.org/10.1002/adma.201806082

39. W. Liu, C. Yi, L. Li, S. Liu, Q. Gui et al., Designing polymer-in-salt electrolyte and fully infiltrated 3D electrode for integrated solid-state lithium batteries. Angew. Chem. Int. Ed. **60**, 12931–12940 (2021). https://doi.org/10.1002/anie.202101537

40. H. Sun, X. Xie, Q. Huang, Z. Wang, K. Chen et al., Fluorinated poly-oxalate electrolytes stabilizing both anode and cathode interfaces for all-solid-state Li/NMC811 batteries. Angew. Chem. Int. Ed. **60**, 18335–18343 (2021). https://doi.org/10.1002/anie.202107667

41. J. Mi, J. Ma, L. Chen, C. Lai, K. Yang et al., Topology crafting of polyvinylidene difluoride electrolyte creates ultra-long cycling high-voltage lithium metal solid-state batteries. Energy Storage Mater. **48**, 375–383 (2022). https://doi.org/10.1016/j.ensm.2022.02.048

42. Y.-F. Huang, T. Gu, G. Rui, P. Shi, W. Fu et al., A relaxor ferroelectric polymer with an ultrahigh dielectric constant largely promotes the dissociation of lithium salts to achieve high ionic conductivity. Energy Environ. Sci. **14**, 6021–6029 (2021). https://doi.org/10.1039/D1EE02663A

43. C. Dai, M. Weng, B. Cai, J. Liu, S. Guo et al., Ion-conductive crystals of poly(vinylidene fluoride) enable the fabrication of fast-charging solid-state lithium metal batteries. Energy Environ. Sci. **17**, 8243–8253 (2024). https://doi.org/10.1039/d4ee03467h

44. W. Yang, Y. Liu, X. Sun, Z. He, P. He et al., Solvation-tailored PVDF-based solid-state electrolyte for high-voltage lithium metal batteries. Angew. Chem. Int. Ed. **63**, e202401428 (2024). https://doi.org/10.1002/anie.202401428

45. H. Cheng, D. Li, B. Xu, Y. Wei, H. Wang et al., Amorphous silicon nitride induced high dielectric constant toward long-life solid lithium metal battery. Energy Storage Mater. **53**, 305–314 (2022). https://doi.org/10.1016/j.ensm.2022.09.003

46. B.-H. Kang, S.-F. Li, J. Yang, Z.-M. Li, Y.-F. Huang, Uniform lithium plating for dendrite-free lithium metal batteries: role of dipolar channels in poly(vinylidene fluoride) and PbZr$_x$Ti$_{1-x}$O$_3$ interface. ACS Nano **17**, 14114–14122 (2023). https://doi.org/10.1021/acsnano.3c04684

47. Z. Luo, W. Li, C. Guo, Y. Song, M. Zhou et al., Two-dimensional silica enhanced solid polymer electrolyte for lithium metal batteries. Particuology **85**, 146–154 (2024). https://doi.org/10.1016/j.partic.2023.04.002

48. K. Yang, L. Chen, J. Ma, C. Lai, Y. Huang et al., Stable interface chemistry and multiple ion transport of composite electrolyte contribute to ultra-long cycling solid-state LiNi$_{0.8}$Co$_{0.1}$Mn$_{0.1}$O$_2$/lithium metal batteries. Angew. Chem. Int. Ed. **60**, 24668–24675 (2021). https://doi.org/10.1002/anie.202110917

49. L. Wu, F. Pei, D. Cheng, Y. Zhang, H. Cheng et al., Flame-retardant polyurethane-based solid-state polymer electrolytes enabled by covalent bonding for lithium metal batteries. Adv.

Funct. Mater. **34**, 2310084 (2024). https://doi.org/10.1002/adfm.202310084

50. T. Deng, L. Cao, X. He, A.-M. Li, D. Li et al., *In situ* formation of polymer-inorganic solid-electrolyte interphase for stable polymeric solid-state lithium-metal batteries. Chem **7**, 3052–3068 (2021). https://doi.org/10.1016/j.chempr.2021.06.019

51. H. Wang, H. Cheng, D. Li, F. Li, Y. Wei et al., Lithiated copper polyphthalocyanine with extended π-conjugation induces LiF-rich solid electrolyte interphase toward long-life solid-state lithium-metal batteries. Adv. Energy Mater. **13**, 2204425 (2023). https://doi.org/10.1002/aenm.202204425

52. P. Shi, J. Ma, M. Liu, S. Guo, Y. Huang et al., A dielectric electrolyte composite with high lithium-ion conductivity for high-voltage solid-state lithium metal batteries. Nat. Nanotechnol. **18**, 602–610 (2023). https://doi.org/10.1038/s41565-023-01341-2

53. W. Stöber, A. Fink, E. Bohn, Controlled growth of monodisperse silica spheres in the micron size range. J. Colloid Interface Sci. **26**, 62–69 (1968). https://doi.org/10.1016/0021-9797(68)90272-5

54. N. Meng, Y. Ye, Z. Yang, H. Li, F. Lian, Developing single-ion conductive polymer electrolytes for high-energy-density solid state batteries. Adv. Funct. Mater. **33**, 2305072 (2023). https://doi.org/10.1002/adfm.202305072

55. Z. Gadjourova, Y.G. Andreev, D.P. Tunstall, P.G. Bruce, Ionic conductivity in crystalline polymer electrolytes. Nature **412**, 520–523 (2001). https://doi.org/10.1038/35087538

56. X. Huang, S. Huang, T. Wang, L. Zhong, D. Han et al., Polyether-b-amide based solid electrolytes with well-adhered interface and fast kinetics for ultralow temperature solid-state lithium metal batteries. Adv. Funct. Mater. **33**, 2300683 (2023). https://doi.org/10.1002/adfm.202300683

57. M. Li, H. An, Y. Song, Q. Liu, J. Wang et al., Ion-dipole-interaction-induced encapsulation of free residual solvent for long-cycle solid-state lithium metal batteries. J. Am. Chem. Soc. **145**, 25632–25642 (2023). https://doi.org/10.1021/jacs.3c07482

58. J. Chen, X. Deng, Y. Gao, Y. Zhao, X. Kong et al., Multiple dynamic bonds-driven integrated cathode/polymer electrolyte for stable all-solid-state lithium metal batteries. Angew. Chem. Int. Ed. **62**, e202307255 (2023). https://doi.org/10.1002/anie.202307255

59. X. Xie, Z. Wang, S. He, K. Chen, Q. Huang et al., Influencing factors on Li-ion conductivity and interfacial stability of solid polymer electrolytes, exampled by polycarbonates, polyoxalates and polymalonates. Angew. Chem. Int. Ed. **62**, e202218229 (2023). https://doi.org/10.1002/anie.202218229

60. Y. Wang, P. Yuan, X.X. Liu, S. Feng, M. Cao et al., Sacrificial NH_4HCO_3 inhibits fluoropolymer/garnet interfacial reactions toward 1mS cm^{-1} and 5V-level composite solid electrolyte. Adv. Funct. Mater. **34**, 2405060 (2024). https://doi.org/10.1002/adfm.202405060

61. Y. Hu, L. Li, H. Tu, X. Yi, J. Wang et al., Janus electrolyte with modified Li$^+$ solvation for high-performance solid-state lithium batteries. Adv. Funct. Mater. **32**, 2203336 (2022). https://doi.org/10.1002/adfm.202203336

62. M. Zhou, R. Liu, D. Jia, Y. Cui, Q. Liu et al., Ultrathin yet robust single lithium-ion conducting quasi-solid-state polymer-brush electrolytes enable ultralong-life and dendrite-free lithium-metal batteries. Adv. Mater. **33**, e2100943 (2021). https://doi.org/10.1002/adma.202100943

63. H. Li, Y. Du, Q. Zhang, Y. Zhao, F. Lian, A single-ion conducting network as rationally coordinating polymer electrolyte for solid-state Li metal batteries (adv.energy mater. 13/2022). Adv. Energy Mater. **12**, 2270054 (2022). https://doi.org/10.1002/aenm.202270054

64. Q. Liu, R. Liu, Y. Cui, M. Zhou, J. Zeng et al., Dendrite-free and long-cycling lithium metal battery enabled by ultrathin, 2D shield-defensive, and single lithium-ion conducting polymeric membrane. Adv. Mater. **34**, e2108437 (2022). https://doi.org/10.1002/adma.202108437

65. Y. Zhai, W. Hou, M. Tao, Z. Wang, Z. Chen et al., Enabling high-voltage "superconcentrated ionogel-in-ceramic" hybrid electrolyte with ultrahigh ionic conductivity and single Li$^+$-ion transference number. Adv. Mater. **34**, 2205560 (2022). https://doi.org/10.1002/adma.202205560

66. X. Shan, M. Morey, Z. Li, S. Zhao, S. Song et al., A polymer electrolyte with high cationic transport number for safe and stable solid Li-metal batteries. ACS Energy Lett. **7**, 4342–4351 (2022). https://doi.org/10.1021/acsenergylett.2c02349

67. X. Zuo, Y. Cheng, L. Xu, R. Chen, F. Liu et al., A novel thioctic acid-functionalized hybrid network for solid-state batteries. Energy Storage Mater. **46**, 570–576 (2022). https://doi.org/10.1016/j.ensm.2022.01.045

68. L. Qiao, S. Rodriguez Peña, M. Martínez-Ibañez, A. Santiago, I. Aldalur et al., Anion π-π stacking for improved lithium transport in polymer electrolytes. J. Am. Chem. Soc. **144**, 9806–9816 (2022). https://doi.org/10.1021/jacs.2c02260

69. Z. Tian, L. Hou, D. Feng, Y. Jiao, P. Wu, Modulating the coordination environment of lithium bonds for high performance polymer electrolyte batteries. ACS Nano **17**, 3786–3796 (2023). https://doi.org/10.1021/acsnano.2c11734

70. X.-X. Wang, L.-N. Song, L.-J. Zheng, D.-H. Guan, C.-L. Miao et al., Polymers with intrinsic microporosity as solid ion conductors for solid-state lithium batteries. Angew. Chem. Int. Ed. **62**, e202308837 (2023). https://doi.org/10.1002/anie.202308837

71. T. Deng, Q. Han, J. Liu, C. Yang, J. Wang et al., Vertically aligned hollow mesoporous silica rods enabling composite polymer electrolytes with fast ionic conduction for lithium metal batteries. Adv. Funct. Mater. **34**, 2311952 (2024). https://doi.org/10.1002/adfm.202311952

72. Y. Yuan, Z. Zhang, Z. Zhang, K.-T. Bang, Y. Tian et al., Highly conductive imidazolate covalent organic frameworks with ether chains as solid electrolytes for lithium metal batteries. Angew. Chem. Int. Ed. **63**, e202402202 (2024). https://doi.org/10.1002/anie.202402202

73. X. Zhan, M. Li, X. Zhao, Y. Wang, S. Li et al., Self-assembled hydrated copper coordination compounds as ionic conductors

for room temperature solid-state batteries. Nat. Commun. **15**, 1056 (2024). https://doi.org/10.1038/s41467-024-45372-2

74. Y. Dong, P. Wen, H. Shi, Y. Yu, Z.-S. Wu, Solid-state electrolytes for sodium metal batteries: recent status and future opportunities. Adv. Funct. Mater. **34**, 2213584 (2024). https://doi.org/10.1002/adfm.202213584

75. Z. Cuihong, Investigation of W-doped P2-$Na_{0.6}Li_{0.27}Mn_{0.73}O_2$ cathode materials for sodium-ion batteries. Energy Storage Sci. Technol. **13**, 3731–3741 (2024). https://doi.org/10.19799/j.cnki.2095-4239.2024.0511

76. J. Yin, Y.S. Zhang, H. Liang, W. Zhang, Y. Zhu, Synthesis strategies of hard carbon anodes for sodium-ion batteries. Mater. Rep. Energy **4**, 100268 (2024). https://doi.org/10.1016/j.matre.2024.100268

Publisher's Note Springer Nature remains neutral with regard to jurisdictional claims in published maps and institutional affiliations.